

Platinum Monolayer on IrFe Core–Shell Nanoparticle Electrocatalysts for the Oxygen Reduction Reaction

Kotaro Sasaki · Kurian A. Kuttyiel · Dong Su · Radoslav R. Adzic

Published online: 19 April 2011
© Springer 2011

Abstract We synthesized high activity and stability platinum monolayer on IrFe core–shell nanoparticle electrocatalysts. Carbon-supported IrFe core–shell nanoparticles were synthesized by chemical reduction and subsequent thermal annealing. The formation of Ir shells on IrFe solid-solution alloy cores has been verified by scanning transmission electron microscopy coupled with energy-loss spectroscopy (EELS) and in situ X-ray absorption spectroscopy. The Pt monolayers were deposited on IrFe core–shell nanoparticles by galvanic replacement of underpotentially deposited Cu adatoms on the Ir shell surfaces. The specific and Pt mass activities for the ORR on the Pt monolayer on IrFe core–shell nanoparticle electrocatalyst are 0.46 mA/cm² and 1.1 A/mg_{Pt}, which are much higher than those on a commercial Pt/C electrocatalyst. High durability of Pt_{ML}/IrFe/C has also been demonstrated by potential cycling tests. These high activity and durability observed can be ascribed to the structural and electronic interaction between the Pt monolayer and the IrFe core–shell nanoparticles.

Keywords Platinum monolayers · Oxygen reduction · Core–shell nanoparticles · Iridium · Iron · Electrocatalysis

Introduction

New electrocatalysts for proton electrolyte membrane fuel cells are highly desired, because the principal drawbacks for cathode catalysts such as slow kinetics for oxygen reduction reaction (ORR), high Pt loading, and poor long-term stability are still persistent in preventing their widespread application [1–4]. We demonstrated that Pt monolayer electrocatalysts (e.g., Pt_{ML}/Pd/C) can be a promising approach to solve these problems [5–9] since all these new electrocatalysts exhibited higher Pt activity in ORR in comparison with those of commercial Pt/C electrocatalysts. Their properties such as activity and durability, depend *inter alia* on the integrity of Pt monolayer as well as the nature of substrate materials such as their sizes, compositions, and structures [10]. To further reduce the total loading of noble metals, new non-noble metal–noble-metal core–shell nanoparticles have been employed as substrates for Pt monolayer [11, 12]. The choice of metals for the shell and core of bimetallic nanoparticles is based on the segregation properties of the two metals [13, 14] as well as their electronic and strain-inducing effects on a Pt monolayer [15, 16].

In this communication, we present a new method of synthesizing carbon-supported IrFe core–shell nanoparticles comprising IrFe alloy cores completely covered with Ir shells. The procedure is facile and amenable to large-scale synthesis. Iridium is known as one of the most stable elements against corrosion [17]; thus, an Ir shell can protect non-noble metals such as Ni in cores from oxidation/dissolution. The new core–shell nanoparticle acts as an improved support for a Pt monolayer, which showed the higher activity of ORR (Table 1) as well as the enhanced stability than those of a commercial Pt/C catalyst.

K. Sasaki · K. A. Kuttyiel · R. R. Adzic (✉)
Chemistry Department, Brookhaven National Laboratory,
Upton, NY 11973, USA
e-mail: adzic@bnl.gov

D. Su
Center for Functional Nanomaterials,
Brookhaven National Laboratory,
Upton, NY 11973, USA

Table 1 Lists of Pt and noble-metal mass activities of the Pt_{ML}/IrFe/C electrocatalyst at 0.90 V/reversible hydrogen electrode as well as those from Pt nanoparticles with a diameter of 4 nm

Pt _{ML} /IrFe/C	Commercial Pt/C (4 nm)			
Pt mass activity ($j/A\ mg_{Pt}^{-1}$)	Noble-metal mass activity ($j/A\ mg_{NM}^{-1}$)	Specific activity ($j/mA\ cm^{-2}$)	Pt mass activity ($j/A\ mg_{Pt}^{-1}$)	Specific activity ($j/mA\ cm^{-2}$)
1.1	0.36	0.46	0.20	0.24

Experimental

The carbon-supported iridium and iron core–shell nanoparticles were prepared as follows. An equal molar ratio of $(NH_4)_2IrCl_6$ and $FeCl_2 \cdot 4H_2O$ salts was mixed with high-area Vulcan XC72R carbon black to obtain a loading of 30 wt.% total metal. The mixture was dissolved in Millipore water, and the salts were then reduced by adding $NaBH_4$. It was washed and rinsed with Millipore water, and then dried. The sample was annealed at 600 °C under 15% H_2/Ar gas for 1 h in a tube furnace. The annealed sample was immersed in 0.5 M H_2SO_4 for a couple of hours to dissolve Fe precipitates on Ir and carbon-support surfaces, and then washed, rinsed, and dried again. Chemical analysis of the resultant IrFe sample was carried out using energy-dispersive X-ray equipped with a JEOL JEM2100F transmission electron microscope. The mean mole ratio of Fe to Ir (x_{Fe}/x_{Ir}) determined from 12 particles was 0.62 with a standard deviation of 0.22.

Pt monolayers were then deposited on the IrFe nanoparticle surfaces on a glassy carbon disk by the galvanic displacement by Pt of an underpotentially deposited (UPD) Cu monolayer [5–9]. After the deposition of a Cu UPD monolayer from 50 mM $CuSO_4$ in a 0.10 M H_2SO_4 solution, the electrode covered with this Cu adlayer was placed into a 1.0 mM K_2PtCl_4 in 50 mM H_2SO_4 solution in an Ar atmosphere. After a 1–2-min immersion to completely replace Cu by Pt, the electrode was rinsed again. All these operations were carried out in a multi-compartment cell in a N_2 atmosphere that prevents the oxidation of Cu adatoms in contact with O_2 . The electrode was covered by a small amount of a Nafion solution and dried in air as described above, before rotating disk electrode measurements.

XRD measurements on the IrFe nanoparticles were taken with a Phillips 3100 diffractometer using Cu K α radiation (1.54056 Å). Samples for analysis were obtained by loading the slurries onto a glass slide, followed by drying them in air. The diffraction patterns were collected from 30° to 80° at a scanning rate of 0.6°/min, with a step size of 0.02°.

Hitachi aberration-corrected scanning transmission electron microscope (HD-2700C) at the Center for Functional Nanomaterials, Brookhaven National Laboratory (BNL)

was used. For this study, we used a 1.4 Å electron probe with a probe current of ~50 pA. The microscope is equipped with a cold-field emission electron source with an energy resolution of 0.35 eV. The carbon-supported nanoparticles were dispersed in water and one drop of the slurry was deposited on a carbon-covered copper grid (EMS, Hatfield, PA).

In situ X-ray absorption spectroscopy (XAS) measurements using an electrochemical cell were undertaken at the National Synchrotron Light Source (NSLS), BNL at the X19A beamline. The IrFe sample (working electrode), a proton exchange membrane (Nafion 117, DuPont Chemical Co., DE), and a Pt thin foil (counter electrode) were sandwiched and clamped tightly by the two acrylic plastic bodies. Each plastic body has an X-ray window. The electrolyte was 1 M $HClO_4$ and an Ag/AgCl leak-free electrode was used as a reference electrode. All potentials in this paper are quoted with respect to the reversible hydrogen electrode. The measurements were carried out at the Ir L₃ edge (11,215 eV) and Fe K edge (7,112 eV) at different potentials at room temperature. This electrochemical cell was designed for acquiring XAS data in both the transmission and fluorescence modes although the data presented below were obtained in the former. Details of the electrochemical cell, which is a modified version of that described in ref. [18], are given elsewhere [8]. The data acquired by both the electrochemical and thermal cells were processed and analyzed by Athena and Artemis software [19].

Results and Discussion

IrFe Core–Shell Nanoparticles

Figure 1 shows the XRD pattern measured from the IrFe/C nanoparticles using Cu K α radiation (1.54056 Å). There is one pronounced reflection peak observed at $2\theta=42.05^\circ$. No individual peaks for Ir or α -Fe (b.c.c.) were observed (the reflection peaks of (111) and (200) for Ir and (110) for α -Fe are denoted in the figure, respectively), indicating that no single Ir or α -Fe phase particles have been formed. Ir and Fe are known to form a solid-solution alloy (a mixture of Ir and γ -Fe (f.c.c.)) at

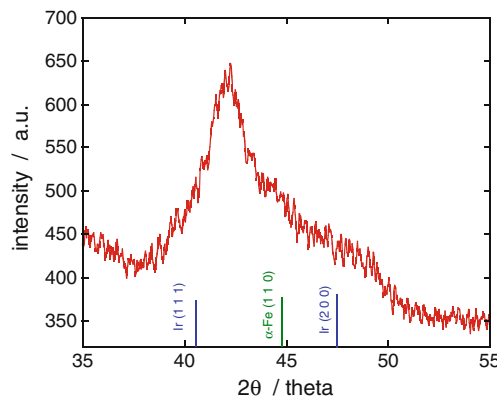


Fig. 1 XRD pattern of carbon-supported IrFe nanoparticles with Cu K α radiation after annealing at 600 °C in H₂ atmosphere for 1 h. Blue and green bars designate the reflections from pure Ir and α -Fe, respectively

concentrations over 62 at.% Ir [20, 21]. The peak in the XRD pattern is indexed between Ir (111) and γ -Fe (111) planes at $2\theta=40.66^\circ$ and 42.92° , respectively, indicating the formation of IrFe solid-solution nanoparticles, possibly with a Fm3m structure with a lattice parameter of $a \approx 3.717$ Å. (We note that both Ir and γ -Fe have an f.c.c. structure and that the lattice parameters for Ir and γ -Fe are 3.839 and 3.6468 Å, respectively [22].) The average size of the IrFe nanoparticles is ca. 3.5 nm, estimated from Scherer's equation [23].

Scanning transmission electron microscopy coupled with energy-loss spectroscopy (STEM-EELS) observations were made with the several nanoparticles. Figure 2 shows (a) a high angle annular dark-field (HAADF) image of a single nanoparticle (ca. 8.6 nm diameter) and (b) comparison of the EELS intensities from the Ir M-edge (2,040 eV) and Fe L-edge (708 eV) obtained by moving the electron probe along the line indicated in Fig. 2a (we note the arbitrary scales of the y axes). In Fig. 2b, it is evident that Ir is enriched (or Fe is depleted) at both edges of the nanoparticle and that the both Ir and Fe are coexisting around the center of nanoparticle; the average thickness of the Ir

shell is ca. 0.75 nm, which corresponds approximately two to three layers of Ir. We consider that the Ir shells formed during annealing at 600 °C as a consequence of segregation of Ir on Fe. Since the XRD pattern show no Fe peaks the cores are considered to comprise IrFe solid-solution alloys.

Figure 3 shows two-dimensional mappings of Fe EELS signal (Fig. 3a) and HAADF intensity (Fig. 3b) on a different IrFe nanoparticle (the HAADF image is depicted in Fig. 3c). The HAADF mapping in Fig. 3b represents predominately the distribution of Ir in the particle since HAADF intensity is approximately proportional to z^2 (z is the atomic number of the constituents) [24] and the Ir mole ratio of the sample is higher than that of Fe. An image overlapping the Fe EELS on the HAADF signals (Fig. 3d) clearly demonstrates the formation of Ir shell on IrFe alloy core. The Ir shell thickness varies depending on the location around the core; but the shell consists of one or two pixels (0.53 nm resolution), which may correspond 2~4 atomic layers of Ir.

Figure 4 shows (a) the in situ X-ray absorption near-edge structure (XANES) and (b) the Fourier transformed extended X-ray absorption fine structure (EXAFS) spectra of the Fe K edge from the IrFe nanoparticles in 1 M HClO₄ at different potentials, together with those from a Fe foil (the thickness ≈ 8 μm). The Fe in the IrFe nanoparticles is considered to be metallic because the edge energy (E_0) shows no shift compared with that of the Fe bulk foil (7,112 eV). The differences between the nanoparticles and the reference foil are apparent in the spectra, indicating that the atomic structure of Fe in the IrFe nanoparticles is significantly different from that in the 3D bulk. As described above, the core may have comprised a IrFe solid-solution alloy, in which iron exists as γ -Fe (f.c.c.) while it does α -Fe (b.c.c.) in a foil at room temperature. In Fig. 4a, the second peak at 7,132 eV in the Fe K edge spectrum increased slightly with increasing potentials, but little change is as a whole observed between the spectra at potentials from 0.41 to 1.11 V. This is more clearly illustrated in the Fourier transformed EXAFS spectra

Fig. 2 **a** HAADF-STEM image of a IrFe nanoparticle and **b** comparison of the EELS intensities for the Ir M-edge and Fe L-edge along the scanned line of the nanoparticle as indicated in (a)

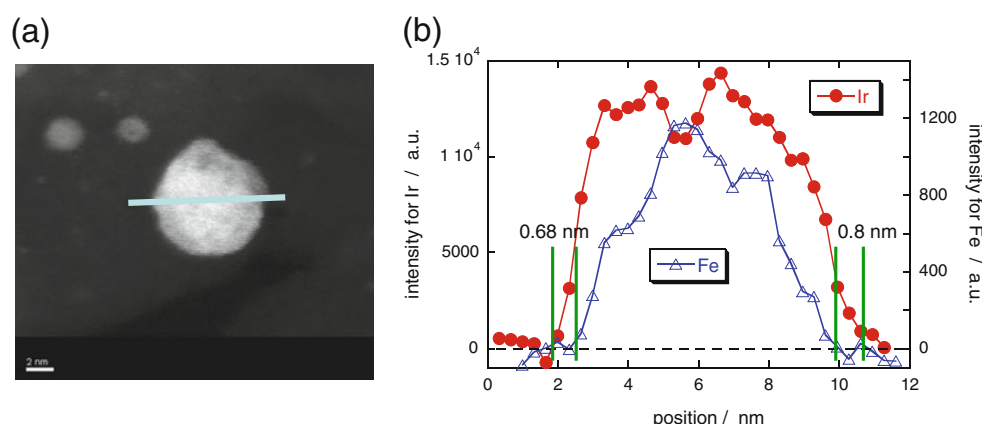
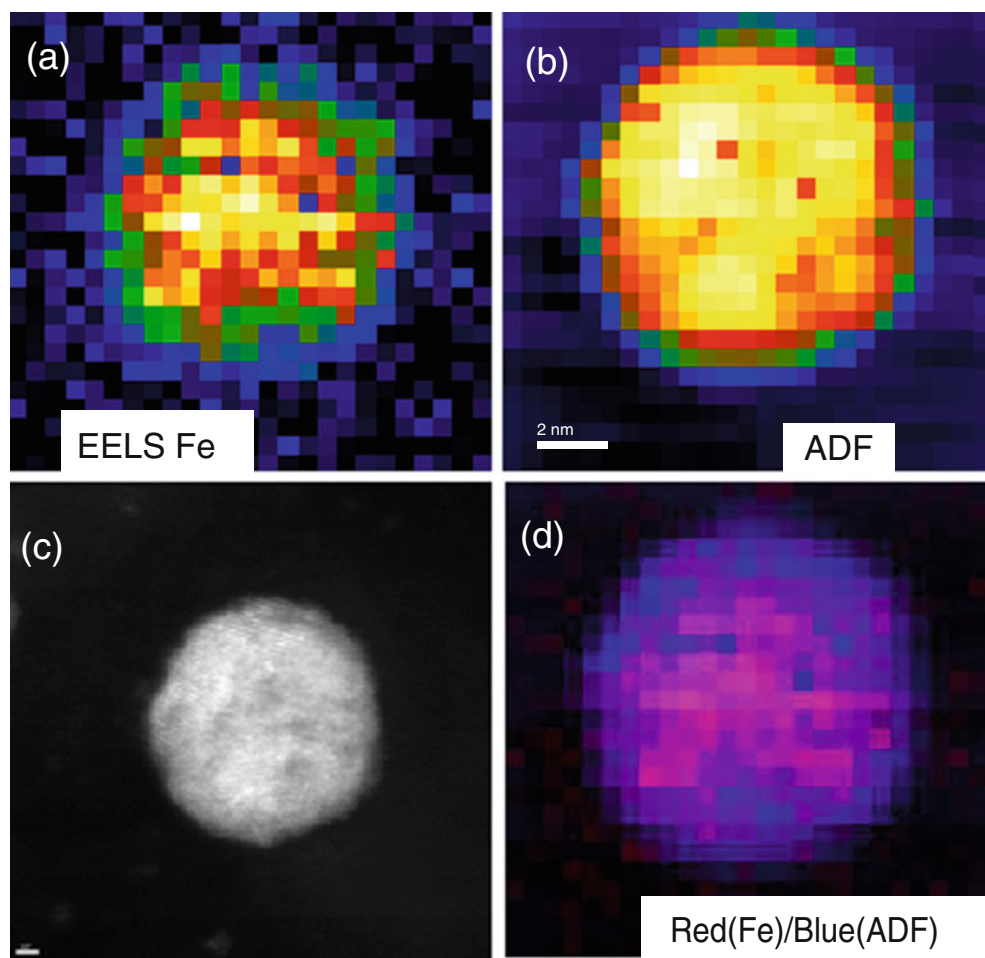


Fig. 3 Two-dimensional mappings of **a** Fe EELS signal and **b** HAADF intensity on **c** a IrFe nanoparticle (HAADF-STEM image). **d** An image overlapping the Fe EELS (red) on the HAADF signal (blue)



(Fig. 4b) in which no characteristic signature of Fe oxides and/or Fe ions is seen even at the high potentials. As shown in Pourbaix diagrams [17], Fe cannot be present in a metallic state when exposed to acid solutions, unless the potential applied is below -0.62 V. The experimental result from the in situ EXAFS indicates that Fe atoms constituting the IrFe cores are not exposed to the electrolyte since the Ir shell completely encapsulates the IrFe core; Fe in the IrFe

solid-solution cores therefore is protected from oxidation or corrosion.

Figure 5 shows (a) the in situ XANES and (b) the Fourier transformed EXAFS spectra of the Ir L₃ edge (11,215 eV) from the IrFe nanoparticles in 1 M HClO₄ at different potentials, together with those from a Ir black (the diameter ≥ 5 μm). In Fig. 5b the highest peak in Ir from the IrFe nanoparticles is displaced to a lower r than

Fig. 4 **a** In situ XANES and **b** the Fourier transformed EXAFS spectra of the Fe K edge from the IrFe nanoparticles in 1 M HClO₄ at different potentials, together with those from an Fe foil (the thickness ≥ 8 μm)

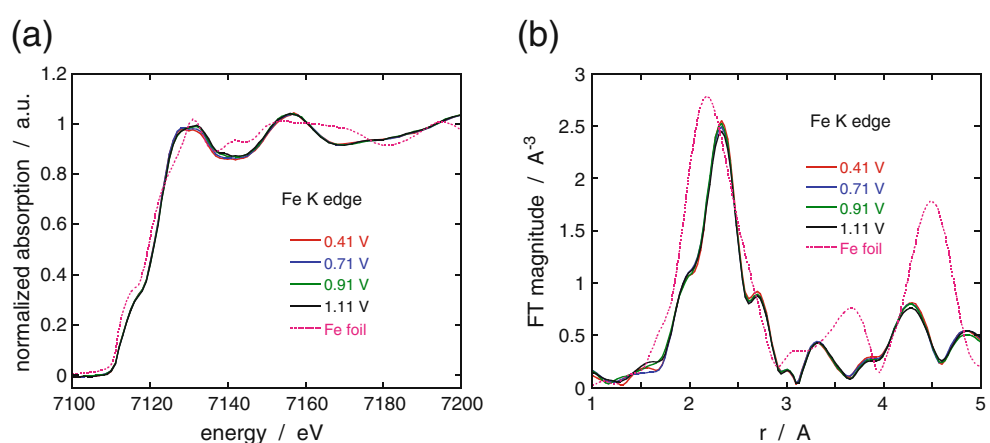
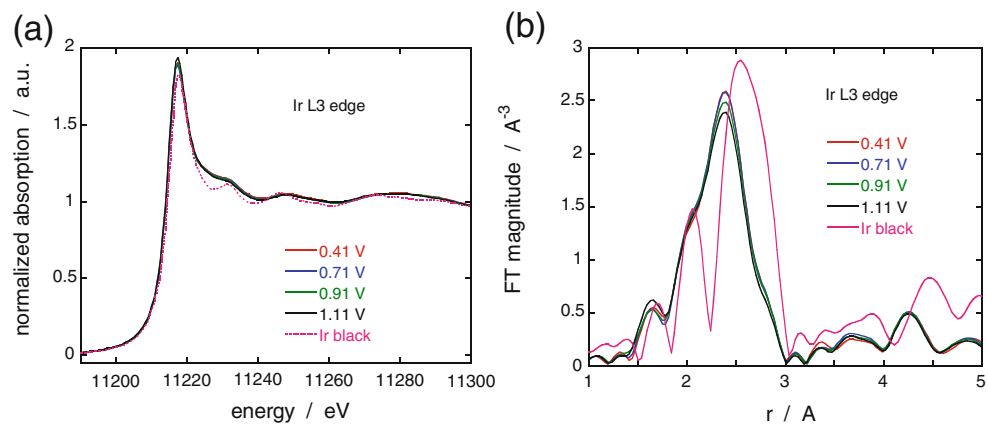


Fig. 5 **a** In situ XANES and **b** the Fourier transformed EXAFS spectra of the Ir L3 edge (11,215 eV) from the IrFe nanoparticles in 1 M HClO₄ at different potentials, together with those from an Ir black (the diameter $\geq 5 \mu\text{m}$)



that from the Ir black. This represents the contraction in the Ir–Ir bonds as a consequence of the formation of IrFe solid-solution alloy cores; the result is in line with that obtained from the XRD measurement (Fig. 1). The results also demonstrated that the Ir spectra did not change significantly with an increase in potential; the white line shows a small rise only at the highest potential of 1.11 V in Fig. 5a, indicating that the oxidation of Ir in the IrFe nanoparticles under elevated potentials is considerably suppressed compared with other observations [7]. This happens predominantly through the geometrical effect, i.e., contraction in the Ir–Ir bond. The Fe-core-induced Ir shell contraction makes the surface less reactive for H₂O oxidation and IrOH formation.

Pt ML on IrFe Core–Shell Nanoparticle Electrocatalysts

Platinum monolayers were deposited on the surfaces of IrFe/C core–shell nanoparticles by replacing an underpotentially deposited copper monolayers. Figure 6 com-

pares polarization curves for the ORR on the IrFe/C and Pt_{ML}/IrFe/C electrocatalysts in oxygen-saturated 0.1 M HClO₄ at a rotation speed of 1,600 rpm. The IrFe/C electrocatalyst shows a half-wave potential ($E_{1/2}$) of 0.627 V, which is slightly higher than that of Ir/C (0.58 V) [25] as a consequence of alloying Ir with Fe; but the activity is much lower than a Pt/C catalyst due to a high binding strength of oxygen at the Ir surface. Placing the platinum monolayers on the surfaces of IrFe nanoparticles yields a substantial increase in ORR activity, as indicated by the high onset potential of O₂ reduction (ca. 1.0 V) as well as the high $E_{1/2}$ (871 mV). The Pt loading was 1.6 nmol (1.9 $\mu\text{g}/\text{cm}^2$).

Figure 7a shows rotating disk electrode (RDE) measurements of the ORR on the Pt_{ML}/IrFe/C electrocatalyst in a 0.1 M HClO₄ solution purged by O₂ at different rotation speeds (400 to 3,025 rpm). Using the same data, the Koutecky–Levich plot, i.e., the inverse current (1/I) plotted as a function of the inverse of the square root of the rotation rate ($\omega^{1/2}$), is presented in Fig. 7b. The linearity and the parallelism of these plots seen in the figure indicate the first-order kinetics with respect to molecular oxygen [26]. The kinetic currents for ORR can be determined from the intercepts of the 1/I axis at $\omega^{1/2}=0$. The Pt specific and mass activities of the Pt_{ML}/IrFe/C electrocatalyst at 0.9 V are determined to be 0.46 mA/cm² and 1.1 A/mg_{Pt}, which are approximately 2 and 5.5 times higher than those of a commercial Pt/C electrocatalyst of 4 nm diameter (0.24 mA/cm² and 0.2 A/mg_{Pt}). Its total precious-metal (Pt+Ir) mass activity is 0.36 A/mg_{Pt+Ir}, which is 1.8 times higher than that of the commercial Pt/C electrocatalyst.

We note that the Pt mass activity on Pt_{ML}/Ir/C is 0.32 A/mg_{Pt} (Kuttiyiel et al., unpublished data) and thus alloying Ir with Fe has a remarkable effect in increasing the ORR activity for the Pt monolayer. It was shown before that the ORR activity of the Pt monolayer on a Ir(1 1 1) surface is inferior to that that of Pt(1 1 1) [27]. Recent studies, however demonstrated that Pt monolayer on Ir–Ni core–shell nanoparticle electrocatalysts show an enhanced

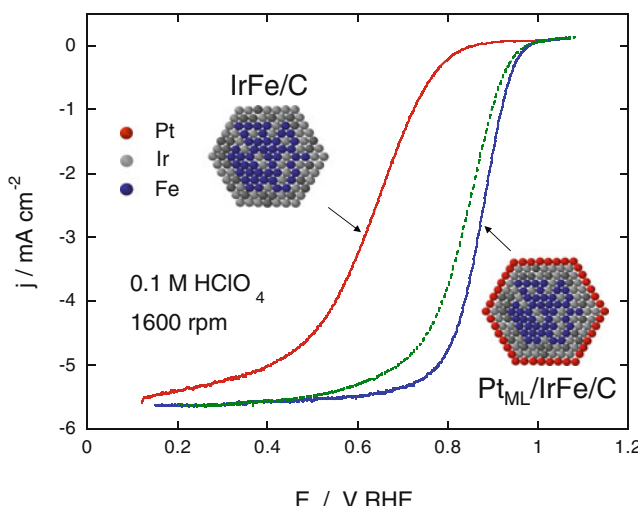
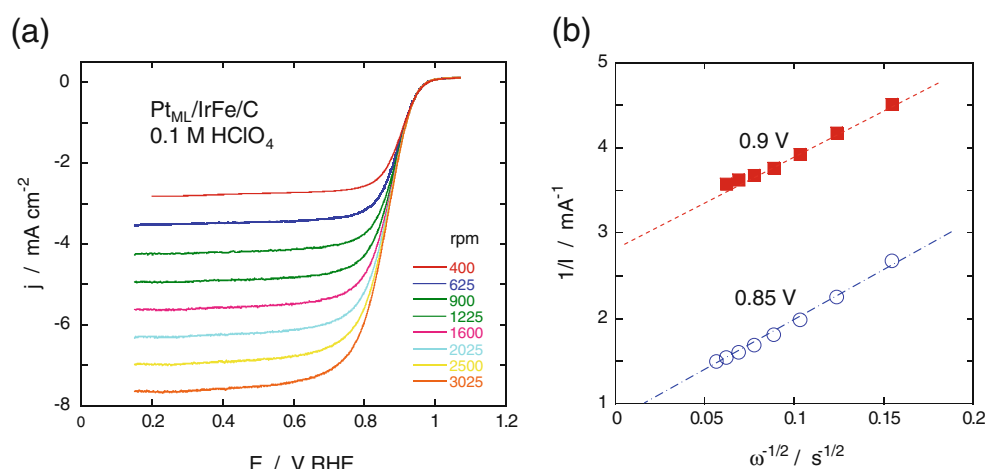


Fig. 6 Comparison of polarization curves for the ORR on the IrFe/C and Pt_{ML}/IrFe/C electrocatalysts in oxygen-saturated 0.1 M HClO₄ at a rotation speed of 1,600 rpm

Fig. 7 **a** RDE measurements of the ORR on the Pt_{ML}/IrFe/C electrocatalyst in a 0.1 M HClO₄ solution purged by O₂ at different rotation speeds (400 to 3,025 rpm) and **b** the Koutecky–Levich plot at potentials of 0.85 and 0.9 V



activity for the ORR compared with that of Pt/C catalyst (Kuttiyiel et al., unpublished data). The effect on Pt monolayer from iridium in a core-shell structure with transition metals such as Fe and Ni, is expected to be different from that from a single crystal Ir surface considering a pronounced effect Fe or Ni core can have on Ir shell.

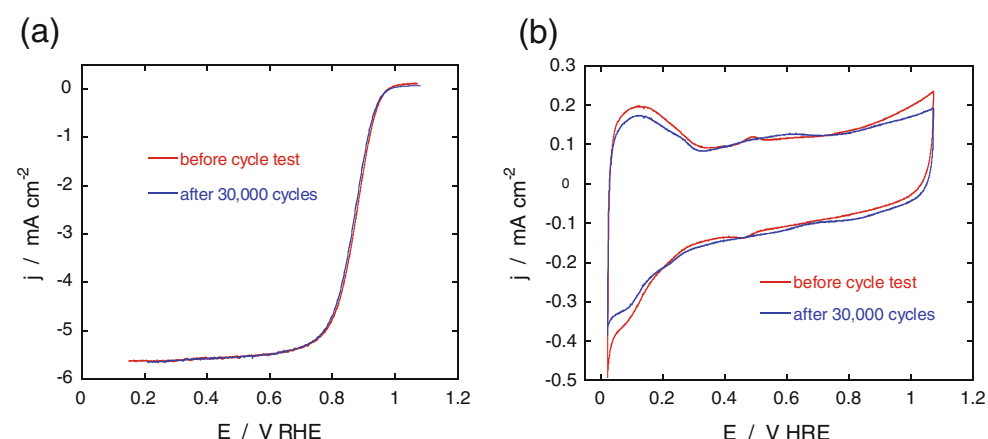
The long-term durability of ORR electrocatalysts is another important requirement for their application in fuel cells. The stability of the Pt_{ML}/IrFe/C was tested by applying potential cycles between 0.60 and 1.0 V at a sweep rate of 50 mV/s at room temperature. Figure 8 shows (a) polarization curves for the ORR and (b) cyclic voltammograms on the Pt_{ML}/IrFe/C electrocatalyst before and after 30,000 cycle test in 0.1 M HClO₄. A decrease in $E_{1/2}$ after the potential cycling is negligibly small (4 mV). The electrocatalyst did not show significant surface loss in Pt (~20%) as indicated by small changes in H₂ adsorption/desorption peaks in the voltammetry curve after the potential cycling test. The degradation in the ORR observed for the Pt_{ML}/IrFe/C electrocatalyst is much smaller compared with a commercial Pt electrocatalyst, which showed a negative shift of 40 mV and a considerable loss in Pt surface area, approximately 45% [28]. The results demon-

strated clearly the improved stability of the the Pt_{ML}/IrFe/C electrocatalyst under potential cycling regime. We envisage that these high activity and durability observed can be ascribed to the structural and electronic interaction between the Pt monolayer and the IrFe core–shell nanoparticles.

Conclusions

We synthesized carbon-supported IrFe core–shell nanoparticles by chemical reduction and subsequent thermal annealing as a new support for Pt monolayer. The formation of Ir shells on IrFe solid-solution alloy cores has been verified using several experimental methods. The Pt monolayers were deposited on IrFe core–shell nanoparticles by galvanic replacement of UPD Cu adatoms on the Ir shell surfaces. The specific and Pt mass activities for ORR on the Pt monolayer on IrFe core–shell nanoparticle electrocatalyst are much higher than those on commercial Pt/C electrocatalysts. High durability of Pt_{ML}/IrFe/C has also been demonstrated using potential cycling tests. Given high activity and stability of this electrocatalyst and its ultralow Pt content, it can be of considerable interest for the application in fuel cell cathodes. In addition, the data

Fig. 8 **a** Polarization curves for the ORR (sweep rate, 10 mV/s) and **b** cyclic voltammograms (sweep rate, 20 mV/s) on the Pt_{ML}/IrFe/C electrocatalyst before and after 30,000 cycle test in 0.1 M HClO₄. The potential was cycled between 0.60 and 1.0 V at a sweep rate of 50 mV/s at room temperature



illustrate a possibility for designing electrocatalysts based on non-noble–noble metal core shell nanoparticles as support for Pt.

Acknowledgements This work is supported by the US Department of Energy, Divisions of Chemical and Material Sciences under contract no. DE-AC02-98CH10886. Beamlines X19A at the NSLS are supported in part by the Synchrotron Catalysis Consortium, US Department of Energy grant no. DE-FG02-05ER15688.

References

1. S. Gottesfeld, T.A. Zawodzinski, in *Advances in Electrochemical Science and Engineering*, vol. 5, ed. by R.C. Alkire, D.M. Kolb (Wiley, Weinham, 1997), p. 195
2. W. Vielstich, A. Lamm, H.A. Gasteiger, in *Handbook of Fuel Cells—Fundamentals, Technology and Applications* (Wiley, Chichester, 2003)
3. H.A. Gasteiger, S.S. Kocha, B. Sompalli, F.T. Wagner, *Appl. Catal. B* **56**, 9 (2005)
4. R.R. Adzic, in *Frontiers in Electrochemistry*, vol. 5, *Electrocatalysis*, ed. by J. Lipkowski, P.N. Ross (VCH Publishers, New York, 1998), p. 197
5. R.R. Adzic, J. Zhang, K. Sasaki, M.B. Vukmirovic, M.H. Shao, J. X. Wang, A.U. Nilekar, M. Mavrikakis, *Top. Catal.* **46**, 249 (2007)
6. J. Zhang, Y. Mo, M.B. Vukmirovic, R. Klie, K. Sasaki, R.R. Adzic, *J. Phys. Chem. B* **108**, 10955 (2004)
7. J. Zhang, M.B. Vukmirovic, K. Sasaki, A.U. Nilekar, M. Mavrilakis, R.R. Adzic, *J. Am. Chem. Soc.* **127**(36), 12480 (2005)
8. K. Sasaki, J.X. Wang, H. Naohara, N. Marinkovic, K. More, H. Inada, R.R. Adzic, *Electrochim. Acta* **55**, 2645 (2010)
9. K. Sasaki, H. Naohara, Y. Cai, Y. Choi, P. Liu, M.B. Vukmirovic, J.X. Wang, R.R. Adzic, *Angew. Chem. Int. Ed.* **49**, 8602 (2010)
10. J.X. Wang, H. Inada, L. Wu, Y. Zhu, Y. Choi, P. Liu, W.-P. Zhou, R.R. Adzic, *J. Am. Chem. Soc.* **131**, 17298 (2009)
11. M.H. Shao, K. Sasaki, N.S. Marinkovic, L. Zhang, R.R. Adzic, *Electrochem. Commun.* **9**, 2848 (2007)
12. K. Gong, D. Su, R.R. Adzic, *J. Am. Chem. Soc.* **132**, 14364 (2010)
13. A.V. Ruban, H.L. Skriver, J.K. Nørskov, *Phys. Rev. B* **50**, 15990 (1998)
14. E. Christoffersen, P. Liu, A. Ruban, H.L. Skriver, J.K. Nørskov, *J. Catal.* **199**, 23 (2001)
15. B. Hammer, J.K. Nørskov, *Adv. Catal.* **45**, 71 (2000)
16. M. Mavrikakis, B. Hammer, J.K. Nørskov, *Phys. Rev. Lett.* **81**, 2819 (1998)
17. M. Pourbaix, in *Atlas of Electrochemical Equilibria in Aqueous Solutions*, (Pergamon/CEBELCOR, Oxford, 1966), pp. 307–321/373–377
18. J. McBreen, W.E. O’Grady, K.I. Pandya, R.W. Hoffman, D.E. Sayers, *Langmuir* **3**, 428 (1987)
19. B. Ravel, M. Newville, *Synchrotron Radiat.* **12**, 537 (2005)
20. ASM Alloy Phase Diagrams Center (2007). Available at: <http://www.asminternational.org/asmenterprise/apd>
21. J.W. Niemantsverdriet, A.A. van der Kraan, *Surf. Interface Anal.* **9**, 221 (1986)
22. W.B. Pearson, in *Handbook of Lattice Spacing’s and Structures of Metals and Alloys*, vol. 2 (Pergamon, New York, 1967), pp. 592–705
23. B.D. Cullity, S.R. Stock, in *Elements of X-Ray Diffraction*, 3rd edn. (Prentice-Hall, Englewood Cliffs, 2001), pp. 167–171
24. M. Weyland, *Top. Catal.* **21**, 175 (2002)
25. K. Lee, L. Zhang, J. Zhang, *J. Power Sources* **170**, 291 (2007)
26. N.A. Anastasijevic, V.B. Vesovic, R.R. Adzic, *J. Electroanal. Chem.* **229**, 305 (1987)
27. J.L. Zhang, M.B. Vukmirovic, Y. Xu, M. Mavrikakis, R.R. Adzic, *Angew. Chem. Int. Ed.* **44**, 2132 (2005)
28. J. Zhang, K. Sasaki, E. Sutter, R.R. Adzic, *Science* **315**, 220 (2007)